Journal of Directed Energy, **2**, Summer 2006, 59–70

Analysis of Thermo-Mechanical Failure Initiation in Tensioned Aluminum Strips Under Irradiation from an IR Heat Source

Jesse McClure and Michael C. Larson*

Mechanical Engineering Department, Tulane University, New Orleans, Louisiana 70118

When a thin, tensioned specimen is irradiated by an IR beam, the temperature of the irradiated zone may increase rapidly and induce large thermal gradients between the heat-affected zone and the surrounding material. The material within the heated zone loses strength, lowering the threshold for rupture. However, the material in the heated zone also softens and expands, thereby relieving a portion of the applied tensile stress, which is taken up by the surrounding material. This redistribution of the load increases the likelihood of cracks forming in the high-thermal-gradient areas surrounding the heated zone. Experimental results show that the magnitude of the applied tension plays a key role in determining the tradeoff between these potential failure site locations. As the tension is increased, the crack initiation region shifts laterally away from the center of the heated zone toward the edges of the zone where the temperature is lower but thermal gradients are highest. Dynamic crack growth ensues after a period of relatively slow fracture development, resulting in failure across the width of the specimen. Results from a finite element model are compared to those of the experiments and are used to propose a quantitative predictor of the actual site location of crack initiation for particular load cases.

KEYWORDS: Aluminum, Crack growth, Failure, Fracture, Irradiation

Nomenclature

A	applied heat load upon material surface, W/m^2
C	heat capacity of the heated material, J/kg
c	specific heat of the heated material, $J \cdot g^{-1} \cdot K^{-1}$
E	elastic modulus of material, GPa
J	Bessel function of the first kind
K	thermal conductivity matrix of heated material, $W \cdot m^{-1} \cdot K^{-1}$
k	thermal conductivity of heated material, $W \cdot m^{-1} \cdot K^{-1}$
P	total power incident upon heated area, W
r	radial distance from the center of heated zone, m
S_u	ultimate strength of material, MPa

Received July 19, 2005; revision received March 12, 2006.

*Corresponding author; e-mail: larson@tulane.edu.

S_y	yield strength of material, MPa
T	temperature of material, K
V_0	initial volume of heated material, m^3
Y	Bessel function of the second kind
α	thermal linear expansion coefficient, $K^{-1} \cdot 10^6$
β	volume expansion coefficient, K^{-1}
ΔT	temperature from the initial state, K
ΔV	overall change in volume due to thermal expansion, m^3
ρ	density of the heated material, kg/m^3

1. Introduction

The rapid heating of metals due to intense laser irradiation results in large temperature gradients within the body. These gradients lead to the buildup of thermal stresses and strains surrounding the irradiated spot, resulting in stress waves and thermal shock waves.[4] These can lead to failure long before actual melt-through occurs, leading to different failure mechanisms. Keshun et al. studied the thermal buckling of precompressed plates and shells and showed that the buckling resistance was greatly reduced when the plates and shells were irradiated by a laser heat source.[5] Buckling can occur at irradiances much lower than required for melting. Zhou et al. found that the bulging can even occur in the direction opposite the laser source under certain conditions.[11] Huang and Duan used these data to show a linear relationship between specimen thickness and critical laser power density required to induce buckling.[3] Zhang et al. conducted work to determine the effect of specimen width on the failure mode of thin pretensioned strips. The results showed that for widths on the same order of magnitude as the spot size, the strips would fail by necking, while for thicker strips the thermal stresses would dominate and result in a buckling failure.[9] Morita discussed laser-induced cracks in unstressed ceramics generated due to thermal shock.[6] Thermally induced cracks are not normally found in unstressed ductile metals subjected to laser irradiation due to their higher relative toughness when compared to ceramics; however, under certain loading conditions cracks can be initiated in ductile metals. Wei and Batra used a continuum damage mechanics model to analyze the effects of laser irradiation on a prestressed aluminum 2024 bar. Results showed that the coupled thermo-mechanical effects could result in rapid failure of the specimen.[8] However, the analysis assumed a constant temperature throughout the bar, which neglects the thermal stresses occurring due to high-temperature gradients surrounding the laser spot. These large gradients can result in the magnification of tensile stresses near the edge of the irradiated spot, resulting in potential crack initiation. Zhou et al. studied the effects on a preexisting crack under tensile stress subjected to laser irradiation. They discovered that as a result of the intense heating at the center of the crack, the crack surfaces come into contact due to thermal expansion.[10] This phenomenon could then be modeled as two separate cracks at the edges of the heated zone that dominate the failure mechanism. In a specimen without an existing precrack, the same stresses arise due to intense heating, and the site of crack initiation can be influenced by both the tensile load and magnitude of the irradiative heat load.

2. Theoretical Background

The general three-dimensional heat conduction equation is given by the solution

$$\rho C \frac{\partial T}{\partial t} = \frac{\partial}{\partial x}\left(K \frac{\partial T}{\partial x}\right) + \frac{\partial}{\partial y}\left(K \frac{\partial T}{\partial Y}\right) + \frac{\partial}{\partial z}\left(K \frac{\partial T}{\partial z}\right) + A(x, y, z, t), \tag{1}$$

where density ρ, heat capacity C, and thermal conductivity K are functions of both position x and temperature T. The function A represents the applied heat load, i.e., that of the incident IR radiation.

If we consider the case of a circular heat spot that is small compared with the in-plane dimensions of a thin sheet, the problem can be considered that of the surface heating of a semi-infinite plate of a finite thickness. Because of the small thickness of the specimen, the heat source can be assumed to heat the right circular cylinder through the thickness of the specimen located under the spot. This results in a constant temperature distribution through the thickness and causes the temperature to depend only on time and radial distance r from the spot. Under the given assumptions, the general solution for the temperature distribution $T(r,t)$ for $r > A$ is given by Carslaw and Jaeger[2]:

$$T(r,t) = \frac{-P\varepsilon}{\pi^2 AKl}\int_0^\infty (1-\exp[-\kappa u^2 t]) \times \left[\frac{J_0(ur)Y_1(uA) - Y_0(uA)J_1(uA)}{u^2\left[J_1^2(uA)+Y_1^2(uA)\right]}\right]du, \quad (2)$$

where P is equal to the total power impingent upon the area πA^2. J and Y represent Bessel functions of the first and second kind. When the condition $A^2/\kappa t \ll 1$ is true for the given geometry and material properties, the equation can be simplified as

$$T(r,t) = \frac{P\varepsilon}{4\pi Kl}\left[\ln\left(\frac{4\kappa t}{Br^2}\right) + \frac{A^2}{2\kappa t}\ln\left(\frac{4\kappa t}{Br^2}\right) + \frac{1}{4\kappa t}\left(A^2 + r^2 - 2A^2\ln\frac{A}{r}\right)\right], \quad (3)$$

where $B = 1.781$. For the given specimen geometry and properties, the value of $A^2/\kappa t = 0.014$ for $t = 10$. Thus, for the given conditions, the simplified equation (3) is valid as time increases above 10 s.

As the temperature increases, volume thermal expansion occurs according to the equation

$$\Delta V = \beta V_0 \Delta T, \quad (4)$$

where ΔV represents the overall change in volume, β is the volume expansion coefficient, V_0 is the initial volume, and ΔT is the temperature change from the initial state. This expansion can result in thermal stresses in the body. These stresses combine with the applied uniaxial stress, resulting in a unique stress field that can initiate cracks and result in the failure of the specimen.

3. Experimental Problem Description

The specimen is a thin dogbone, shown in Fig. 1, with overall length of 25.4 cm (10 in.) and a grip width of 10.2 cm (4 in.). At the neck, the specimen is 3 in. wide. The thickness of the specimen is 0.635 mm (0.025 in.). The test pieces are constructed from aluminum 2024-T3. The specimen is then placed under constant load conditions. The tensile testing machine is programmed to maintain constant load despite elongation of the specimen. Once the desired load is achieved, the IR heat load is applied.

One side of the specimen is subjected to infrared irradiation while the other side is left open to the atmosphere. A circular spot is heated by using an IR heat lamp. To increase thermal coupling into the specimen, a 1.0-cm (0.04-in.)-diameter black spot of high-temperature paint was applied to the target zone.

The profile of the IR source was fairly uniform over the area of the heated spot. At the periphery of the circle, the irradiance values began to drop off quickly, as shown in Fig. 2. The beam profile and irradiance were measured by using a small heat flux sensor having a

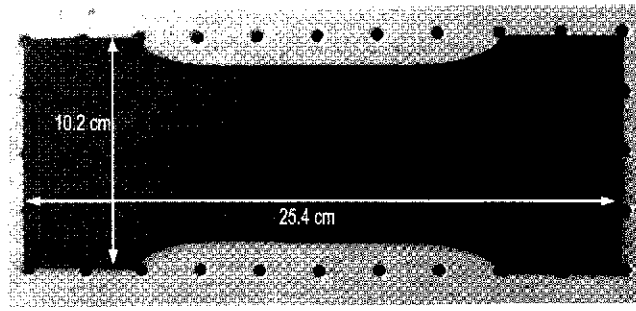

Fig. 1. Dogbone 2024-T3 Al specimen.

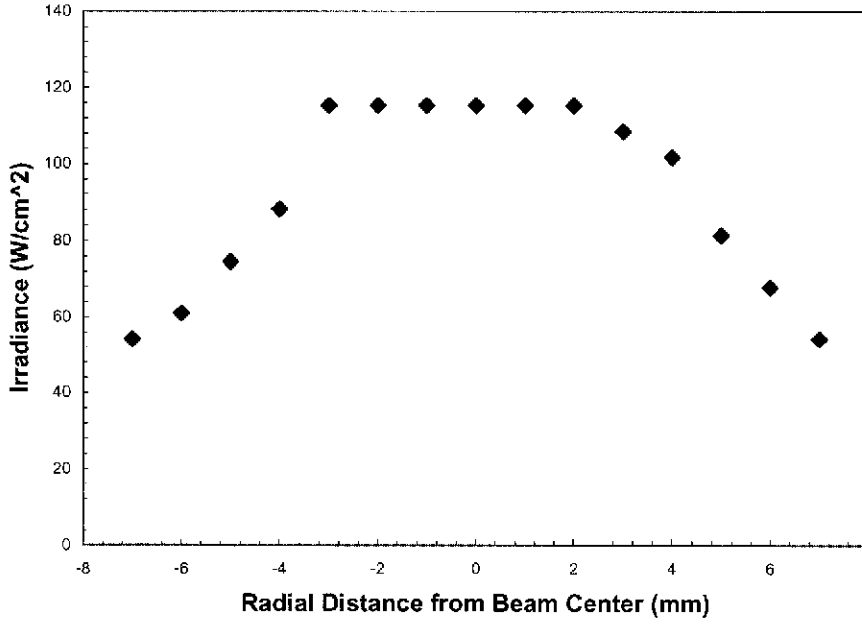

Fig. 2. Measurement of beam irradiance values as a function of distance from the center of the beam.

known absorptivity. With the use of a translation stage, the sensor was moved through the beam and heat flux readings were taken at 1-mm increments.

While the emissivity of the high-temperature black paint is 0.90, the emissivity of the bare aluminum is 0.09, an order of magnitude less. For this reason any IR heating outside of the painted spot is neglected. The heat flux applied by the IR source is assumed to be constant and distributed uniformly around the circular spot. All the energy is assumed to be deposited at the surface, leaving only conduction as a means of heat transfer through the thickness. While the specimen is left exposed to the open atmosphere, no induced flow is allowed around the specimen. For this reason convective heat loss is neglected. Irradiative heat loss from the specimen is also ignored.

Experimental data are gathered by using several devices. The load frame captures load and displacement values with respect to time, which can later be used to determine time to

failure. Temperature data are gathered by using an IR bolometer camera. To increase the emissivity and eliminate reflected IR radiation from the surface, the back of the specimen is painted with high-temperature black paint. Video of the dynamic crack front is captured by using a high-speed charge-coupled device (CCD) camera capable of up to 55,000 frames per second. Using the specimen failure as a time stamp, all three sets of data can be synchronized by moving backward from the fracture event.

4. Computational Results

Figure 3 shows the mesh for a quarter-symmetry, nonlinear finite element model of the specimen shown in Fig. 1. The model was created by using ABAQUS to calculate temperatures, stresses, and strains throughout. The mechanical load consists of a constant applied uniaxial tension applied to the top edge of the specimen. The thermal load is a uniformly heated one-quarter circular spot positioned at the lower-left-hand corner of the specimen. (Superposition of elastic solutions is not appropriate because of the nonlinear temperature-dependent properties of the material.) The temperature-dependent properties of aluminum 2024-T3 used in the simulation can be found in Tables 1 (Ref. 7) and 2 (Ref. 1).

In Fig. 3, the x axis of the specimen is constrained in the y direction due to specimen symmetry. All other degrees of freedom are left unconstrained along this axis. Along the y axis the specimen is constrained from displacement in the x direction due to specimen symmetry. As before, all other degrees of freedom remain unconstrained. It is important to note that both the x and y axes are left unconstrained in the z direction to allow for the specimen to bulge out of plane due to thermal expansion. The upper edge of the specimen is constrained in all directions except displacement in the y direction. This constraint is a result of the specimen grips, which permit translation only in the y direction.

Table 1. Thermophysical properties of aluminum 2024-T3 as a function of temperature[7]

Temperature T, K	Thermal conductivity k, W/m·K	Specific heat c, J/g·K	Thermal linear expansion α, 10^{-6}/K
250	1.14	0.837	20.0
273	1.19	0.858	20.8
293	1.23	0.870	21.6
300	1.24	0.874	21.9
350	1.33	0.904	23.7
400	1.41	0.925	25.1
450	1.60	0.946	26.4
500	1.77	0.975	27.5
550	1.83	1.008	28.4
600	1.85	1.042	29.1
650	1.83	1.079	29.7
700	1.80	1.125	30.0
750	1.76	1.172	30.1
775	1.73	1.197	30.1

Table 2. Mechanical properties of aluminum 2024-T3 as a function of temperature[1]

Temperature T, K	Elastic modulus E, GPa	Possion's ratio	Temperature T, K	Strength, MPa	
				Ultimate	Yield
300	72.4	0.33	297	470	325
400	57.2	0.33	373	422	304
500	48.2	0.33	422	297	249
600	35.4	0.33	477	180	145
700	22.5	0.33	533	97	66
800	5.73	0.33	589	48	35
			644	35	24

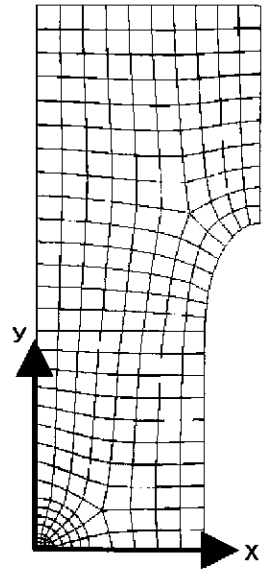

Fig. 3. One-quarter model finite element mesh of dogbone specimen.

To combine the thermal and mechanical effects, ABAQUS coupled temperature-displacement, 20-node standard quadratic brick elements are used in the analysis. The objective of the computational model is to determine the sites of initial yielding within the specimen. For this reason a linear-elastic constitutive model is used in the finite element method (FEM) analysis, with the stiffness varying spatially with the temperature field.

Loads are applied to the element mesh in two steps. First, an evenly distributed uniaxial tension is applied to the top surface of the specimen in the y direction. Once the solution is computed, a heat flux equal to the absorbed radiant flux is applied to the quarter spot located at the bottom-left-hand corner of the model mesh, and both thermal and mechanical reactions are computed. A plot of the temperature distribution across the specimen in the short time domain can be seen in Fig. 4. In the short timescale, the applied heat load does not have time to conduct away from the irradiated spot and there is no appreciable temperature rise at the edges of the specimen within the first second of heating.

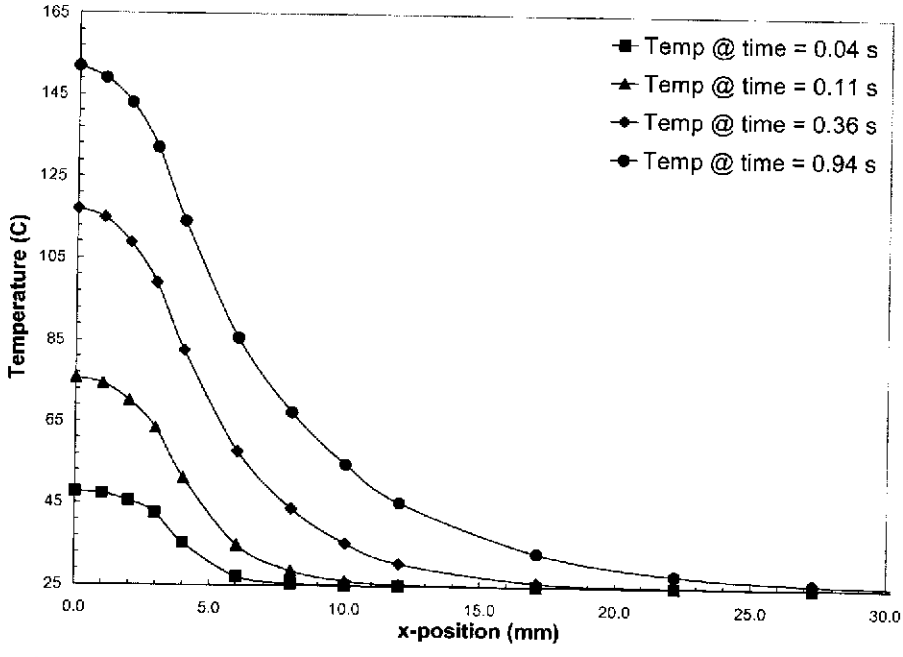

Fig. 4. Computational results of development of temperature gradients along the cross section of the 0.025-in. (0.635-mm)-thick dogbone specimen subjected to 0.40-in. (1-cm)-diameter IR heating at 1 kW/in.^{2} (155 W/cm^2).

The localized temperature increase results in the expansion of the material within the heated spot. As the material expands, the tensile load within the spot is relaxed. This relaxation of stress results in the shedding of the tensile load away from the heated spot toward the specimen periphery. The shift in stress distribution due to the thermal shock can be seen in Fig. 5.

During the first fraction of a second, the von Mises stress at the edge of the heated spot rises rapidly due to the thermal shock. Depending on the initial stress state due to tensile loading, these stresses may exceed the yield stress for the material and lead to ductile yielding. Figure 6 shows a scenario in which the specimen is initially loaded to 90% of the yield strength. Both von Mises stress and temperature-dependent yield stress are plotted as functions of position from the heated spot. Different curves represent different values in time.

The plot shows that at these loading conditions, the yield stress is reached almost instantaneously at the edges of the heated zone. The result is yielding in those regions outside of the heated zone, which can lead to crack nucleation and necking of the material.

Under altered loading the yielding of the specimen occurs at different sites. Figure 7 depicts the scenario in which the specimen is initially loaded to 70% of the yield strength with the identical heat load applied as in Fig. 6. Once again the von Mises and yield stresses are plotted as functions of position from the heated spot. The graph shows that the stress spike due to thermal shock does not approach the room-temperature yield stress of the material.

Figure 8 plots the von Mises and yield stresses as a function of the distance from the center of heating. Yielding does not occur until the heat source has been on for more than

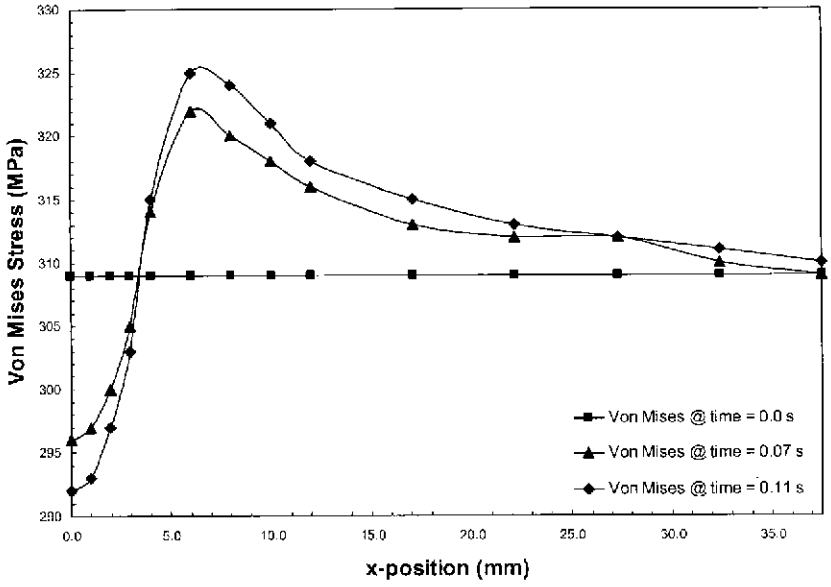

Fig. 5. Computational results of development of von Mises stress distributions along the cross section of the specimen due to rapid localized heating of 0.025-in. (0.635-mm)-thick dogbone specimen at 90% yield subjected to 0.40-in. (1-cm)-diameter IR heating at 1 kW/in.^{2} (155 W/cm^2).

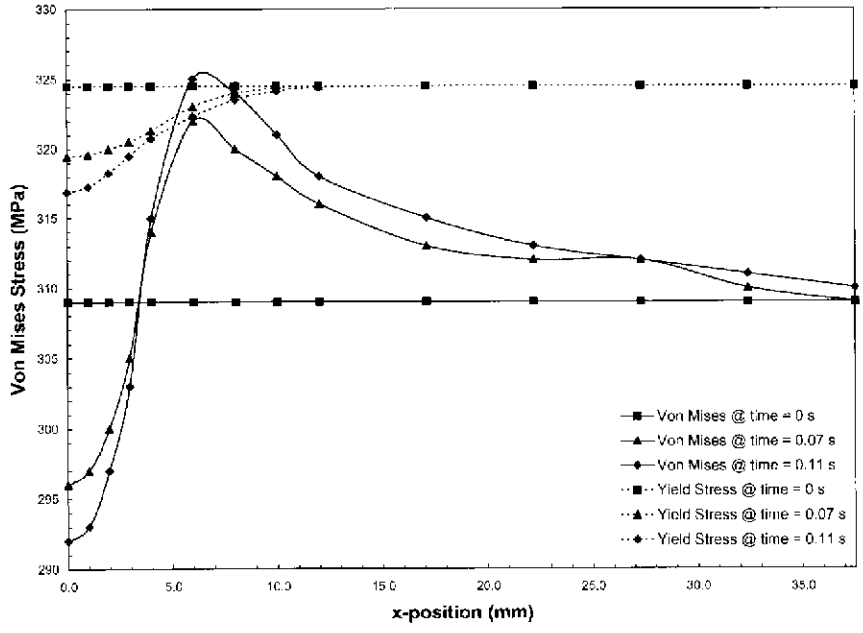

Fig. 6. Computational results of development of von Mises stresses along the cross section of the 0.025-in. (0.635-mm)-thick dogbone specimen at 90% yield subjected to 0.40-in. (1-cm)-diameter IR heating at 1 kW/in.^{2} (155 W/cm^2). Rapid localized heating causes the magnitude to exceed the temperature-dependent yield stress at the flanks of the heated zone.

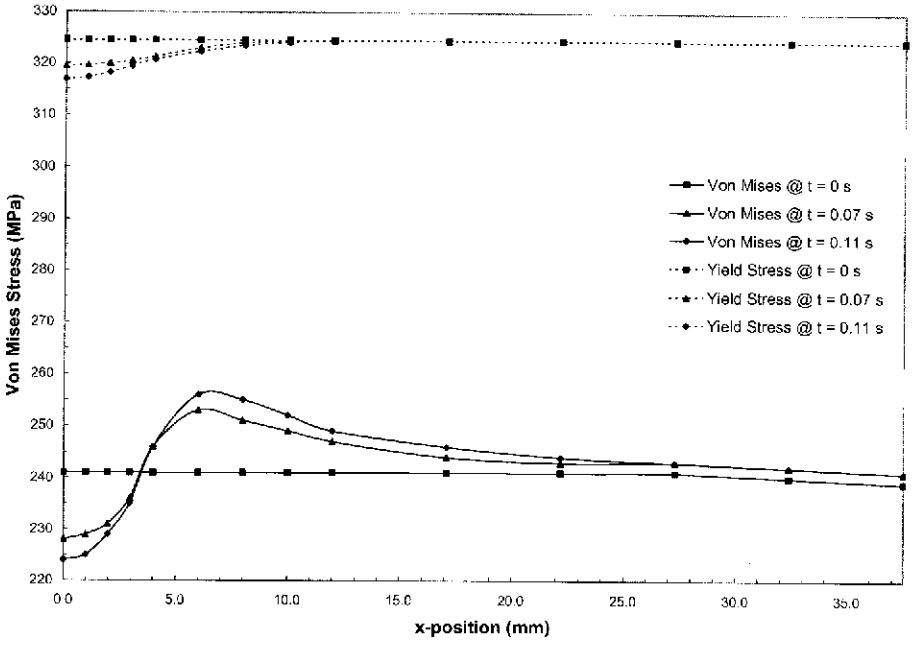

Fig. 7. Computational results of development of von Mises stress distributions along the cross section of the specimen due to rapid localized heating of 0.025-in. (0.635-mm)-thick dogbone specimen at 70% yield subjected to 0.40-in. (1-cm)-diameter IR heating at 1 kW/in.^{2} (155 W/cm^2).

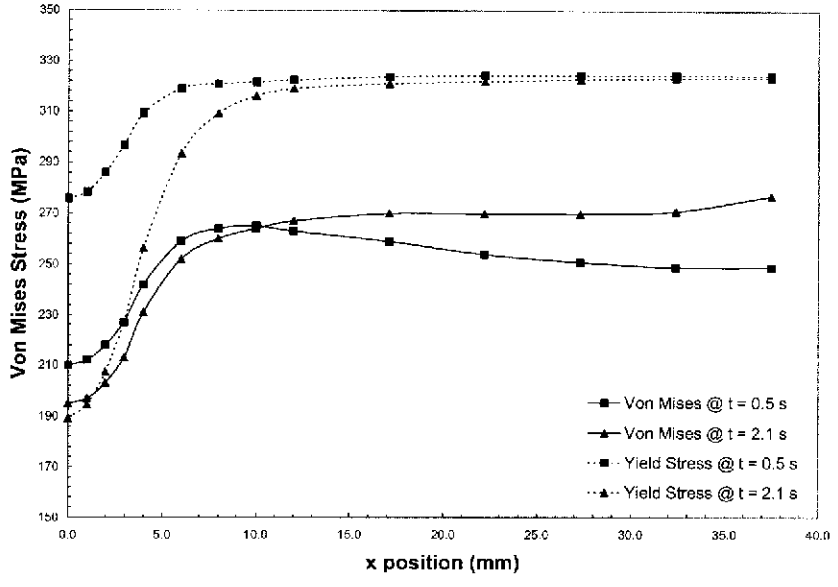

Fig. 8. Computational results of development of von Mises stresses along the cross section of the 0.025-in. (0.635-mm)-thick dogbone specimen at 70% yield subjected to 0.40-in. (1-cm)-diameter IR heating at 1 kW/in.^{2} (155 W/cm^2). The localized heating causes the yield stress to drop below the imposed stress in the center of the heated zone.

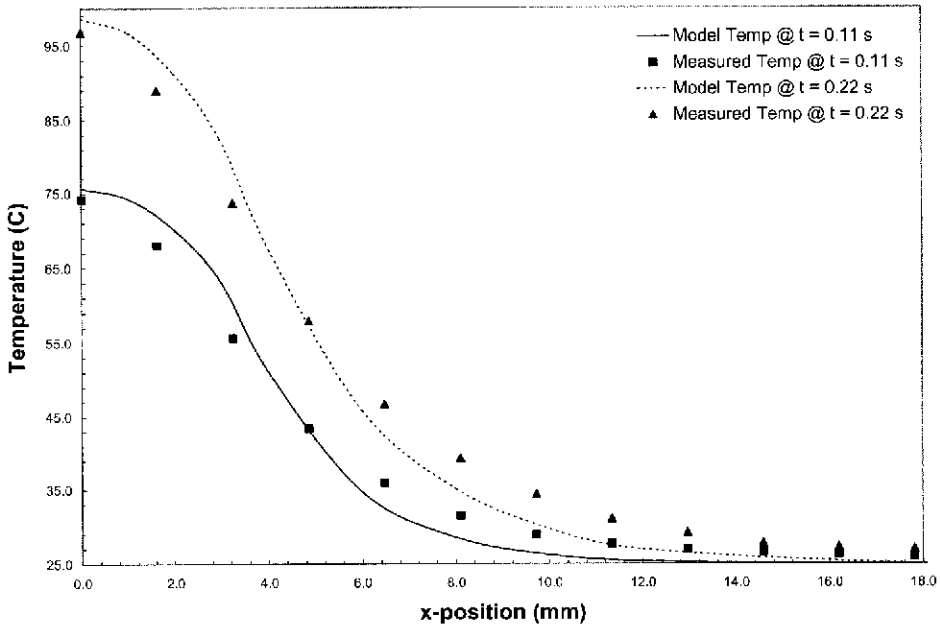

Fig. 9. Computational and measured values for the temperature distribution surrounding the heated zone. X position relates the distance from the center of the heated zone along the x axis.

2 s. Most notable, however, is the location of the yielding. While in the scenario at 90% yield the specimen began to yield at the edges of the heated zone, at 70% the specimen begins to yield at the center of the heated region. This difference is evident in the observed locations of failure initiation in experimental specimens.

5. Experimental Results

Temperature field data are gathered by using the thermal camera. While the two scenarios involve different applied tensile loads, the thermal load is the same for each case. For this reason the thermal field for both situations is identical. Figure 9 plots the temperature as a function of position from the center of the heated zone. It can be seen in the short timescale that the computational temperature field closely resembles that gathered from the thermal camera.

High-speed video is used to capture images at the onset of crack initiation. Figure 10 shows the sites of crack initiation for a specimen subjected to a 90% yield load. In this video frame, it is evident that two distinct cracks exist, separated by a ligament of the softer heated metal. Figure 11 depicts the crack initiation of a specimen subjected to a 70% yield load. The frame clearly shows a single crack that has initiated within the heated zone.

6. Discussion

Stresses were examined in finite element models to identify sites where yielding first occurs after the heat load is applied. These were determined by comparing the von Mises

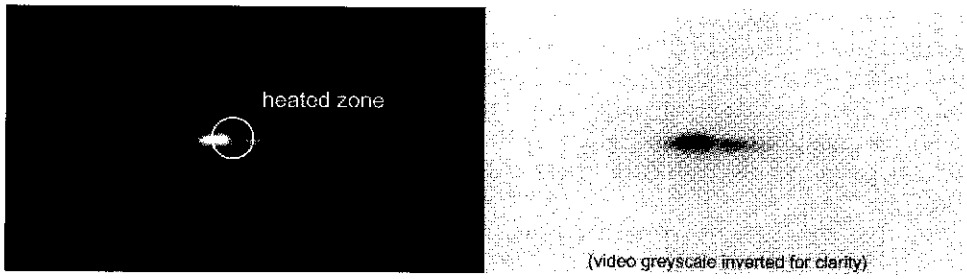

Fig. 10. Frame from high-speed video showing double-site crack initiation for 0.025-in. (0.635-mm)-thick dogbone specimen at 90% yield subjected to 0.40-in. (1-cm)-diameter IR heating at 1 kW/in.^{2} (155 W/cm^2).

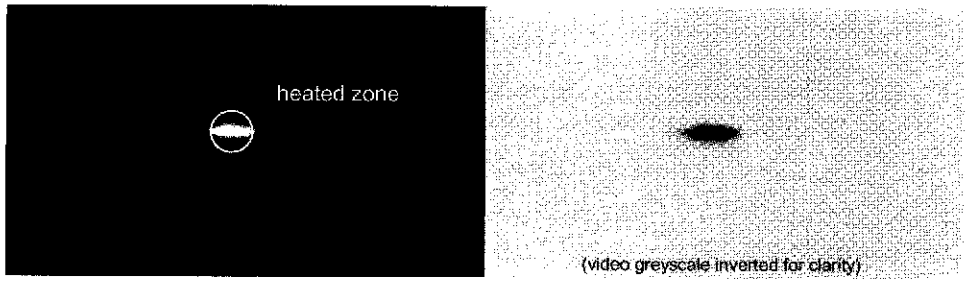

Fig. 11. Frame from high-speed video showing double-site crack initiation for 0.025-in. (0.635-mm)-thick dogbone specimen at 90% yield subjected to 0.40-in. (1-cm)-diameter IR heating at 1 kW/in.^{2} (155 W/cm^2).

stresses, which are direct outputs of the model, with the yield stresses that are determined by using the nodal temperatures output by the model.

At the instant this yielding begins to occur, the material begins to deform plastically, resulting in dislocation motion and localized necking of the material. This necking represents a localized defect in the specimen, which leads to potential crack site initiation. In the specimens prestressed to 90% yield, this yielding occurs at the edge of the heated zone, resulting in crack initiation at those edges, as seen in Fig. 9. These sites correspond to the regions shown in Fig. 5 under yielding. For the specimens prestressed to 70% yield, in Fig. 6 it can be seen that yielding does not occur at the edge of the heated zone when the heat load is first applied. Rather, initial yielding occurs at the center of the heated zone, as seen in Fig. 7. This results in crack initiation near the center of the heated spot, as depicted in Fig. 10.

7. Conclusion

A FEM model was constructed to represent the situation of a dogbone of 2024-T3 Al under uniaxial tension being subjected to an IR heat source. Analyzing the changes in the stress field due to the thermal shock, the sites of crack initiation were predicted by using the computational model. Experimental data gathered by using high-speed video confirmed the location of the predicted sites for crack initiation. The comparisons between model and

experiment reveal the importance of accounting for the change in mechanical properties of the irradiated material. The effects of variable heat input from the IR source were not explored, while they certainly would have an effect and will be addressed in future work. The growth of the crack after initiation was not modeled due to extensive computational time, however. Analysis is currently underway to explore using the Crack-Tip-Opening-Angle (CTOA) as a criterion indicative of continued growth of cracks initiated by the thermal loading.

8. Acknowledgment

The authors gratefully acknowledge the support for this project under a contract from the Missile Defense Agency. The contents of this paper, however, do not necessarily reflect the positions of the U.S. Government, and as such, no official endorsement should be inferred.

References

[1]Aluminum Company of America, *Alcoa Structural Handbook*, Pittsburgh, PA (1956).

[2]Carslaw, H.S., and J.C. Jaeger, *Conduction of Heat in Solids*, 2nd ed. Oxford Univ. Press, London and New York (1959).

[3]Huang, C.G., and Z.P. Duan, Appl. Math. Mech. **23**(7), 748 (2002).

[4]Huimin, X., W. Guotao, Z. Daqing, D. Fulong, P. Dietz, Z. Wei, and A. Schmidt, J. Mat. Process. Technol. **82**, 137 (1998).

[5]Keshun, D., J. Zheng, A.W. Davies, and F.W. Williams, AIAA J. **38**, 1789 (2000).

[6]Morita, N., J. Ceramic Soc. Japan, Int. Ed. **101**, 510 (1993).

[7]Touloukian, Y.S., and C. Y. Ho, "Thermophysical Properties of Selected Aerospace Materials," Thermophysical and Electronic Properties Information Center, CINDAS, Purdue Univ. (1977).

[8]Wei, Z.G., and R.C. Batra, J. Thermal Stresses, **26**, 701 (2003).

[9]Zhang, S., Y. Yin, G. Zhang, and Y. Chen, Key Engineer. Mat., **177–180**, 99 (2000).

[10]Zhou, Y.C., Z.M. Zhu, and Z.P. Duan, Int. J. Solids Structures **38**, 5647 (2001).

[11]Zhou, Y.C., Z.P. Duan, and Q.B. Yang, Int. J. Non-Linear Mech. **33**(3), 433 (1998).